Characterization of Noncrystalline Nanomaterials: NMR of Zinc Phosphate as a Case Study

Marcus Roming,[†] Claus Feldmann,*[,†] Yamini S. Avadhut,[‡] and Jörn Schmedt auf der Günne*[,‡]

Institut für Anorganische Chemie, Universität Karlsruhe, Engesserstrasse 15, D-76131 Karlsruhe, Germany, and Institut für Anorganische Chemie, Ludwig-Maximillians-Universität München, Butenandtstrasse 5-13, D-81377 München, Germany

Received March 19, 2008. Revised Manuscript Received July 1, 2008

Zinc phosphate nanoparticles are prepared via a polyol-mediated synthesis. The nanomaterial turns out to be nonagglomerated and very uniform in size and shape, in particular 20 nm in diameter. X-ray powder diffraction analysis and high-resolution transmission electron microscopy indicate as-prepared nanoparticles to be noncrystalline. To investigate the chemical composition (stoichiometry, material homogeneity, amount of ortho-/metaphosphate, water content, type of surface-allocated adsorbents, differentiation of surface/inner core), X-ray diffraction, NMR-spectroscopy, energy-dispersive X-ray analysis, infrared spectroscopy, and thermal analysis are performed. To validate the local structure and composition, we performed ^{1}H, ^{13}C, and ^{31}P magic angle spinning nuclear magnetic resonance spectroscopy and multidimensional homo- and heteronuclear multiple-pulse solid-state NMR experiments. Moreover, $^{31}P\{^{1}H\}$ rotational echo double-resonance experiments for various spin topologies are analyzed analytically and numerically, in order to differentiate between homogeneous nanoparticles and core−shell nanoparticles. The analysis gives a length scale to homogeneity and for bulk materials allows us to differentiate between mono- and dihydrogen phosphates, and phosphate hydrates.

Introduction

State-of-the-art nanometer-scaled materials are typically characterized regarding fundamental issues such as particle size and morphology, size distribution and crystal structure.[1−4] To this end, electron microscopy and atomic force microscopy belong to the most important types of analytical tools. Aiming at a profound analytical characterization, and thereby an even more dedicated knowledge of nanomaterials, additional aspects such as the local chemical composition, the material homogeneity, the differentiation between particle surface and inner core, the type and amount of surface-allocated adsorbents, as well as the presence of a crystalline core and/or a noncrystalline shell/surface are even as important as the primary issues. Moreover, all aspects mentioned are of significant relevance with regard to the expression of different physical properties, including color, magnetism, luminescence, catalysis, and electron or ion conductivity.[1,2,5,6]

In the case of noncrystalline nanomaterials, analytical characterization is even more complicated. Only the use of different and independent methods—strongly encouraging spectroscopic methods—can lead to a well-balanced view. Here, magic angle spinning nuclear magnetic resonance (MAS NMR) spectroscopy is of special importance in order to gain a detailed view of the solid state down to an atomic scale. Indeed, NMR techniques are of rapidly increasing interest with regard to nanostructured materials. Analytical characterization has been yet directed to the inner surface of zeolites,[7] the surface conditioning of catalytically active metal and oxide particles,[8−10] the composition of carbon nanotubes,[11] hydrogen absorption,[12,13] inorganic−organic nano composite,[14,15] as well as doped nanoparticles.[15,17] Although partial aspects of analytical characterization have

* Corresponding author. Phone: 49-721-608-2855 (C.F.); 49-89-2180-77433 (J.S.a.d.G.). Fax: 49-721-608-4892 (C.F.); 49-89-2180-77440 (J.S.a.d.G.). E-mail: feldmann@aoc1.uni-karlsruhe.de (C.F.); gunnej@cup.uni-muenchen.de (J.S.a.d.G.).

[†] Universität Karlsruhe.

[‡] Ludwig-Maximillians-Universität München.

(1) Ozin, G.; Arsenault, A. *Nanochemistry: A Chemistry Approach to Nanomaterials*; RSC Publishing: Cambrige, U.K., 2005.
(2) Klabunde, K. J. *Nanoscale Materials in Chemistry*; Wiley: New York, 2001.
(3) Cushing, B. L.; Kolesnichenko, V. L.; O'Connor, C. J. *Chem. Rev.* **2004**, *104*, 3893.
(4) Park, J.; Joo, J.; Kwon, S. G.; Jang, Y.; Hyeon, T. *Angew. Chem., Int. Ed.* **2007**, *46*, 4630.
(5) Shionoya, S., Yen, W. M., Eds. *Phosphor Handbook*; CRC Press: Boca Raton, FL, 1999.
(6) Minami, T. *Semicond. Sci. Technol.* **2005**, *20*, 35.
(7) Rocha, A. S.; Teixeira da Silva, V.; Eon, J. G.; De Menezes, S. M. C.; Faro, A. C.; Rocha, A. B. *J. Phys. Chem. B* **2006**, *110*, 15803.
(8) Zhang, W. H.; Zhang, X.; Hua, Z.; Harish, P.; Schroeder, F.; Hermes, S.; Cadenbach, T.; Shi, J.; Fischer, R. A. *Chem. Mater.* **2007**, *19*, 2663.
(9) Fiurase, P.; Reven, L. *Langmuir* **2007**, *23*, 2857.
(10) Berrettini, M. G.; Braun, G.; Hu, J. G.; Strouse, G. F. *J. Am. Chem. Soc.* **2004**, *126*, 7063.
(11) Sekhaneh, W.; Katecha, M.; Dettlaff-Weglikowska, U.; Veeman, W. S. *Chem. Phys. Lett.* **2006**, *428*, 143.
(12) Kobayashi, H.; Yamauchi, M.; Kitagawa, H.; Kubota, Y.; Kato, K.; Takata, M. *J. Am. Chem. Soc.* **2008**, *130*, 1828.
(13) Brunklaus, G.; Koch, A.; Sebastiani, D.; Spiess, H. W. *Phys. Chem. Chem. Phys.* **2007**, *9*, 4545.
(14) Schmidt-Rohr, K.; Rawal, A.; Fang, X.-W. *J. Chem. Phys.* **2007**, *126*, 054701.
(15) Jäger, C.; Welzel, T.; Meyer-Zaika, W.; Epple, M. *Magn. Reson. Chem.* **2006**, *44*, 573.
(16) Holland, G. P.; Sharma, R.; Agola, J. O.; Amin, S.; Solomon, V. C.; Singh, P.; Buttry, D. A.; Yarger, J. L. *Chem. Mater.* **2007**, *19*, 2519.

10.1021/cm800805f CCC: $40.75 © 2008 American Chemical Society
Published on Web 08/27/2008

been investigated quite often based on solid state NMR, the number of fundamental studies addressing noncrystalline nanomaterials and including the chemical composition and the morphological structure as most relevant features of a compound is quite limited till now.[18,19] The situation, however, is much more difficult in comparison to crystalline nanomaterials because typical standard methods (e.g., X-ray diffraction, electron microscopy) are only with limited expressiveness. The underlying restrictions are well-known even for noncrystalline bulk materials.[20]

Here, noncrystalline zinc phosphate nanoparticles are prepared and investigated as a case study. Surprisingly, zinc phosphate has not been realized with state-of-the-art quality (e.g., almost monodisperse and nonagglomerated) on the nanoscale till now. Room-temperature solid-state reactions and microemulsion techniques have already been applied, and resulted in $Zn_3(PO_4)_2 \cdot 2H_2O$, 40−50 nm in size with broad size distribution and significant aggregation.[21] In contrast, $Zn_3(PO_4)_2$ as a bulk material is well-known and widely applied, including filler materials (e.g., in glasses, plastics), various aspects of surface conditioning (e.g., anticorrosion pigment, UV-stabilization, flame proofing), catalysis and biomedical applications (e.g., dental cement, bioactive glasses).[22−26] Moreover, bulk $Zn_3(PO_4)_2$ represents a common host lattice for fluorescent materials with $Zn_3(PO_4)_2$:Mn as the most prominent example, which is applied in cathode-ray tubes and as a long lasting phosphor.[27,28] Nanoscale zinc phosphate is here prepared via a polyol-mediated approach.[29,30] To characterize the as-prepared and noncrystalline material, we invoked electron microscopy (SEM, TEM), dynamic light scattering (DLS), gas adsorption (BET), energy dispersive X-ray analysis (EDX), X-ray powder diffraction (XRD), thermal analysis (DTA-TG), and infrared spectroscopy (FT-IR). To investigate the material on an atomic level, ^1H, ^{13}C, and ^{31}P magic angle spinning nuclear magnetic resonance spectroscopy (MAS NMR), including rotational echo double resonance (REDOR) experiments are applied.

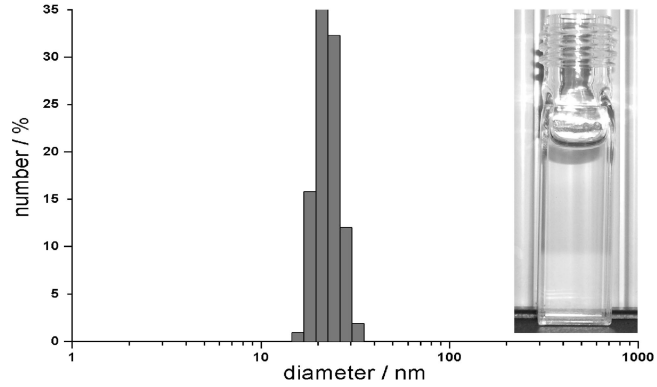

Figure 1. Photo and DLS analysis of as-prepared zinc phosphate particles (resuspended in DEG).

Results and Discussion

(a) Synthesis and Fundamental Characterization. As-prepared zinc phosphate was investigated by applying state-of-the-art analytical tools in order to evaluate particle diameter and morphology, size distribution, and degree of agglomeration. Furthermore, chemical composition and structure as well as the thermal properties and crystallization were verified on the basis of analytical methods that preferentially address crystalline materials.

Synthesis. Nanoscale zinc phosphate with a nominal composition of $Zn_3(PO_4)_2$ was here prepared via a polyol-mediated synthesis. This synthetic approach is a widely applied strategy to fabricate various types of nanomaterials, including elemental metals, oxides, sulfides and fluorides.[29−32] The polyol, which is a multidentate and high-boiling alcohol such as glycerine, ethylene glycol, or diethylene glycol (DEG), first guarantees a sufficient solubility of the starting materials. As a second effect, the generated nanoparticles are colloidally stabilized during precipitation and heating. The latter results in a controlled particle growth and an efficient suppression of agglomeration. The underlying equilibrium between chelation of dissolved cations and surface stabilization of colloidal nanoparticles has to be adjusted carefully for each system and compound.[30−32] Here, the title compound was prepared by mixing solutions of $ZnAc_2 \cdot 2H_2O$ in diethylene glycol (DEG) and $(NH_4)(H_2PO_4)$ in water. For optimal conditions of nucleation, mixing of the starting materials was performed at slightly elevated temperatures (50 °C). Thereafter, the suspension was refluxed for 45 min at 230 °C in order to support a well-controlled particle growth. Because of the high boiling point of the polyols (typically 250−350 °C),[33] heating can be performed pressureless. Subsequent to synthesis, suited washing processes, and drying, the colorless solid was redispersed in DEG. The resulting suspension was with a slightly opalescent appearance and colloidally stable within weeks (Figure 1.)

Particle Size and Morphology. Particle diameter and size distribution of the as-prepared zinc phosphate were determined via dynamic light scattering (DLS) and scanning

(17) Reyes-Garcia, E. A.; Sun, Y.; Reyes-Gill, K.; Raferty, D. *J. Phys. Chem.* **2007**, *111*, 2738.
(18) Rawal, A.; Wei, X.; Akinc, M.; Schmidt-Rohr, K. *Chem. Mater.* **2008**, *20*, 2583.
(19) Veith, M.; Mathur, S.; Kareiva, A.; Jilavi, M.; Zimmer, M.; Huch, V. J. *Mater. Chem.* **1999**, *9*, 3069.
(20) Tilley, R. J. D., *Understanding Solids: The Science of Materials*; Wiley, Chichester, U.K., 2004.
(21) Yuan, A. Q.; Liao, S.; Tong, Z. F.; Wu, J.; Huang, Z. Y. *Mater. Lett.* **2006**, *60*, 2110.
(22) Seth, A.; van Ooij, W. J.; Puomi, P.; Yin, Z.; Ashirgade, A.; Bafna, S.; Shivane, C. *Prog. Org. Coat.* **2007**, *58*, 136.
(23) Mostashari, S. M.; Darsaraei, A. *Int. J. Chem.* **2005**, *15*, 89.
(24) Tagiyev, D. B.; Aliyev, A. M.; Mamedov, N. D.; Fatullayeva, S. S. *Surf. Sci. Catal., A* **2004**, *154*, 1049.
(25) Milutinovic-Nikolic, A. D.; Medic, V. B.; Vukovic, Z. M. *Dent. Mater.* **2007**, *23*, 674.
(26) Day, R. M.; Boccaccini, A. R. *J. Biomed. Mater. Res., A* **2005**, *73*, 73.
(27) Smith, A. L. *J. Electrochem. Soc.* **1951**, *98*, 363.
(28) Wang, J.; Wang, S.; Su, Q. *J. Mater. Chem.* **2004**, *14*, 2569.
(29) Toneguzzo, P.; Viau, G.; Acher, O.; Guillet, F.; Bruneton, E.; Fievet, F. *J. Mater. Sci.* **2000**, *35*, 3767.
(30) Feldmann, C.; Jungk, H. O. *Angew. Chem., Int. Ed.* **2001**, *40*, 359.
(31) Feldmann, C. *Adv. Funct. Mater.* **2003**, *13*, 101.
(32) Roming, M.; Trampert, K.; Feldmann, C. *Small* **2006**, *2*, 1248.
(33) Lide, D. R., Ed. *Handbook of Chemistry and Physics*; CRC Press: Boca Raton, FL, 2006.

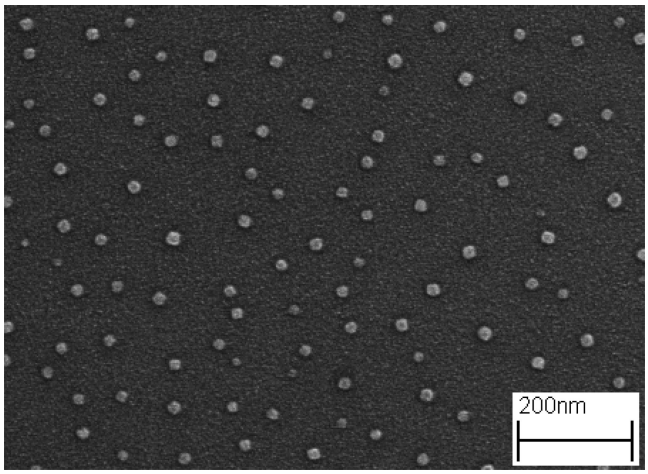

Figure 2. SEM image displaying as-prepared zinc phosphate particles.

electron microscopy (SEM). DLS analysis results in an average hydrodynamic diameter of 20(2) nm and is evidence of the absence of any significant agglomeration (Figure 1). The latter is even more interesting because the particles were centrifuged, dried, and redispersed. Again, the efficient stabilization of nanoscale materials via the polyol as the liquid phase has been confirmed. SEM images confirm the presence of nonagglomerated particles with a narrow size distribution (Figure 2.) Here, a statistical evaluation based on 460 particles resulted in an average diameter of 21(3) nm. This value is in good agreement with DLS analysis. For further characterization of the powder material, the specific surface of as-prepared zinc phosphate was measured. Via the Brunauer−Emett−Teller (BET) method, a value of 140 $m^2\ g^{-1}$ was derived. With the assumption of spherical, nonporous particles, and considering the density of bulk $Zn_3(PO_4)_2$ (3.998 g cm^{-3}),[33] this value is in accordance with both the observed particle diameter as well as the presence of a nonagglomerated nanoparticles.

Material Crystallinity and Chemical Composition. Former investigations have shown nanoscale materials synthesized in high-boiling alcohols often to be well-crystallized.[27−29] In contrast, nanoscale zinc phosphate with a nominal composition $Zn_3(PO_4)_2$ turned out to be noncrystalline even after heating to reflux (45 min at 230 °C). This is proven for powder samples based on X-ray powder diffraction as well as with electron diffraction based on bundles of particles (Figure 3.) HR-TEM (high-resolution transmission electron microscopy) on the one hand confirms the particle diameter as given by DLS and SEM and on the other hand again gives evidence that individual particles are noncrystalline (Figure 3). Because as-prepared zinc phosphate is noncrystalline, additional measures were included to determine its chemical composition. First, energy-dispersive X-ray analysis (EDX) evidence the presence of Zn, P, and O as well as a Zn:P ratio of 3:2, which corresponds well with the expected composition $Zn_3(PO_4)_2$. Second, infrared spectroscopy was invoked (Figure 4.) The characteristic vibrational bands can be related to the $(PO_4)^{3-}$ anion and correspond to reference spectra of $Zn_3(PO_4)_2$: $\nu(PO_4^{3-})$ = 1066 cm^{-1} (ref.: 1050

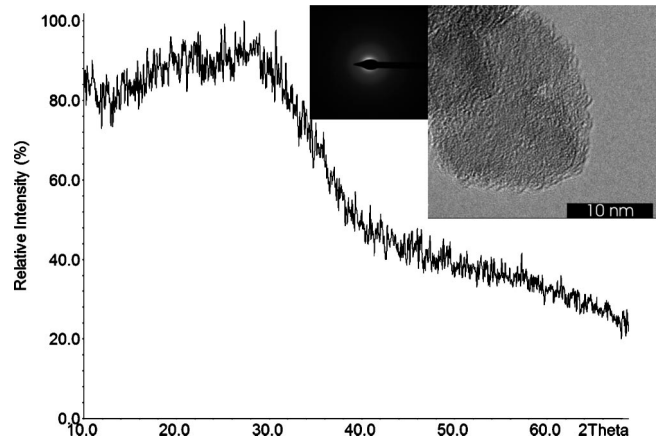

Figure 3. XRD, SAED, and HR-TEM image of as-prepared zinc phosphate nanoparticles.

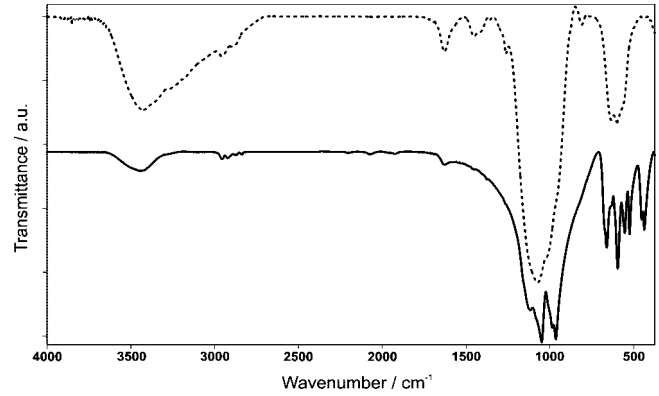

Figure 4. FT-IR spectra of zinc phosphate nanoparticles: as-prepared sample (dotted), annealed sample (3 h at 600 °C, straight).

cm^{-1}), $\delta(PO_4^{3-})$ = 596 cm^{-1} (ref.: 600 cm^{-1}).[34] On the basis of previous investigations, additional bands can be attributed to DEG (ν(OH): 3500−3000 cm^{-1}, ν(CH): 3000−2800 cm^{-1}, ν(CO): superpositioned by $\nu(PO_4^{3-})$) and H_2O (ν(OH): 3500−3000 cm^{-1}, $\delta(OH_2)$: 1624 cm^{-1}).[35,36] Finally, typical chemical shift values of DEG, water and the orthophosphate anion were observed with ^1H and ^{31}P solid-state NMR spectra (see below).

Thermal Behavior and Crystallization. $Zn_3(PO_4)_2$ as a bulk compound has been described with three different structural modifications: α-$Zn_3(PO_4)_2$ is characterized by two crystallographically independent zinc sites with a distorted tetrahedral coordination; β-$Zn_3(PO_4)_2$, in contrast, exhibits three independent zinc sites with tetrahedral, octahedral, and quadratic pyramidal coordination; γ-$Zn_3(PO_4)_2$ is only obtained when doped with additional ions such as Mn^{2+}, Mg^{2+}, or Cd^{2+}, and contains two zinc sites with distorted octahedral and trigonal bipyramidal coordination.[37] To elucidate the thermal behavior and a potential crystallization of the as-prepared noncrystalline zinc phosphate, we performed differential thermal analysis (DTA) and thermogravimetry (TG). To this end, a certain weight loss was observed to occur with two steps: 3% between room temperature and 180 °C,

(34) Weidlein, J.; Müller, U.; Dehnicke, K. *Schwingungsspektroskopie*; Thieme: Stuttgart, Germany, 1988.
(35) Feldmann, C.; Matschulo, S.; Ahlert, S. *J. Mater. Sci.* **2007**, *42*, 7076.
(36) Buchold, D. H. M.; Feldmann, C. *Chem. Mater.* **2007**, *19*, 3376.
(37) Stephens, J. S.; Calvo, C. *Can. J. Chem.* **1967**, *45*, 2303.

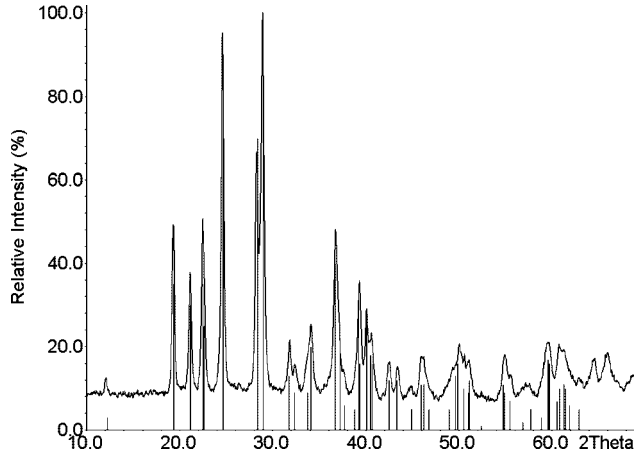

Figure 5. XRD pattern of nanoscale zinc phosphate subsequent to annealing (3 h, 600 °C), with α-$Zn_3(PO_4)_2$ (ICDD 29−1390) added as references.

followed by 7% between 180 and 500 °C. Considering the relevant boiling points as well as the outcome of former investigations,[33,35,36] the first step can be attributed to water and ethanol, the second to DEG. Thermal analysis further exhibits an exothermic DTA signal at 542 °C, which hints to a crystallization of the sample. Subsequent to annealing of as-prepared zinc phosphate for 3 h at 600 °C, XRD pattern indeed show the presence of crystalline α-$Zn_3(PO_4)_2$ as a pure phase (Figure 5.) The finding of a crystalline compound subsequent to the thermal treatment also coincides with a splitting of the vibration bands found in IR-spectra (Figure 4). The latter is in correspondence with the reduced site symmetry of the $[PO_4]^{3-}$ tetrahedra when incorporated in the crystal lattice (Figure 4).[34] IR-spectra further confirm DEG- and H_2O-related vibrations to be almost completely vanished when annealing the powder samples.

(b) Analysis of Local Structure and Structural Models. Taking the so-far presented results into account, we can denote the as-prepared material as a, XRD and electron diffraction amorphous zinc phosphate, which upon heating under weight loss forms crystalline α-$Zn_3(PO_4)_2$. Taking into account the weight loss observed during thermogravimetry, the approximate composition of as-prepared noncrystalline zinc phosphate can be estimated to be $Zn_3(PO_4)_2 \cdot 0.3(DEG) \cdot 0.7(H_2O)$. An interesting question to be answered is if the crystalline α-$Zn_3(PO_4)_2$ is preformed in the as-prepared material. In other words, does the as-prepared material contain a $Zn_3(PO_4)_2$ core, which upon heating is transformed into the crystalline phase? The material would then contain a hydrogen-free core and a shell that might contain significant amounts of DEG ("core−shell model"). The counter hypothesis is a core-free model that has a more or less homogeneous composition throughout ("homogeneous model", Figure 6.)

Solid-state NMR methods can be used to prove and quantify spatial neighborhood of NMR active elements.[34] In the core−shell model, the core region is free of hydrogen atoms, whereas the homogeneous model contains H and P atoms throughout. In solid-state NMR spectroscopy for a homogeneous sample, the spatial connectivity patterns for H and P atoms, for H and H atoms, and for P and P atoms should then all be detectable, i.e., the distances should be

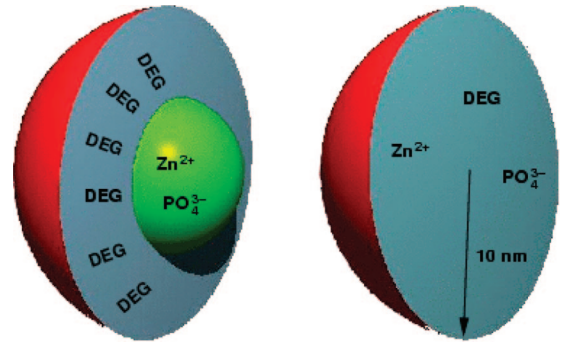

Figure 6. Models for as-prepared zinc-phosphate nanoparticles: (left) core−shell model, (right) core-free model assuming a homogeneous composition throughout.

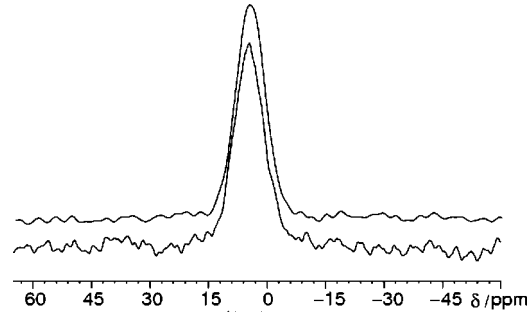

Figure 7. $^{31}P\{^1H\}$ MAS NMR spectra: (top) $^{31}P\{^1H\}$ CP MAS NMR recorded at a sample spinning frequency of 10 kHz with ^1H decoupling at a magnetic field of 4.7 T, a contact time of 5 ms, (bottom) ^{31}P MAS spectrum with direct excitation at 10 kHz sample spinning frequency using a recycle delay of 16384 s and ^1H decoupling.

below one nanometer. Hence we have acquired $^{31}P\{^1H\}$ 2D heteronuclear correlations spectra, $^1H-^1H$ and $^{31}P-^{31}P$ homonuclear double-quantum filtered correlation spectra, and $^{31}P\{^1H\}$-C-REDOR curves.

^{31}P, ^{13}C, and ^1H 1D MAS. Simple 1D ^1H, ^{13}C, and ^{31}P MAS NMR of the zinc phosphate nanoparticles both showed relatively broad resonances (projections on 2D spectra in Figure 10 and Figure 7) that are typical for amorphous samples. The peak at 3.4 ppm in the ^1H NMR spectrum was identified with protons of the methylene group of DEG,[38] the peak at 6.8 ppm could either be due to H_2O and/or the alcohol function of DEG. Because of the flexibility of isotropic chemical shift values for ^1H atoms in hydrogen bonds, we set further assignment aside. In a $^{13}C\{^1H\}$ cross-polarization magic angle spinning (CPMAS) (Supporting Information), we observed peaks at 71.0 and 60.4 ppm, which we assigned to DEG. The observed isotropic and anisotropic ^{31}P chemical shift values are typical for PO_4^{3-} groups, clearly the formation of $P_2O_7^{4-}$ can be ruled out by comparison to literature values [39,40] and reference materials (Table 1). In general, for a diphosphate, the magnitude of the ^{31}P anisotropy of the chemical shift is bigger than that of an orthophosphate. For the ^{31}P isotropic chemical shift there is a trend to lower values the higher the number of bridging

(38) Hesse, M.; Meier, H.; Zeeh. B. *Spektroskopische Methoden in der Organischen Chemie*; Thieme Verlag: Stuttgart, Germany,1991.
(39) Brow, R. K.; Tallant, D. R.; Myers, S. T.; Phifer, C. C. *J. Non-Cryst. Solids* **1995**, *191*, 45.
(40) Hartmann, P.; Vogel, J.; Schnabel, B. *J. Magn. Reson., A* **1994**, *111*, 110.

Table 1. ^{31}P NMR Chemical Shift Parameters and Spin-Lattice Relaxations Times of α-$Zn_3(PO_4)_2$, β-$Zn_3(PO_4)_2$, and As-Prepared Zinc Phosphate Nanoparticles

	δ_{iso} (ppm)	δ_{aniso} (ppm)	η	δ_{11} (ppm)	δ_{22} (ppm)	δ_{33} (ppm)	T_1 (s)
α-$Zn_3(PO_4)_2$	3.9	−36	0.86	37.0	6.4	−31.7	1948
β-$Zn_3(PO_4)_2$	7.6	20	0.62	−8.7	3.8	27.7	946
	2.8	−12	0.92	14.4	3.3	−9.2	742
as-prepared zinc-phosphate	4.8	29	0.8	−21	2	34	48
α-$Zn_2P_2O_7$	−21.2	81	0.0	−21.2	−21.2	59.5	
	−19.1	71	0.36	−32.1	−6.4	52.3	
	−15.9	71	0.38	−29.6	−2.6	55.0	
γ-$Zn_2P_2O_7$	−10.4	81	0.0	−10.3	−10.3	70.9	
	−7.1	75	0.62	−30.8	16.0	68.3	
	−5.5	64	0.15	−10.4	−0.7	58.9	

δ_{11}, δ_{22}, and δ_{33} are the principle axis values. Definitions of δ_{iso}, δ_{aniso}, and η are the same as in SIMPSON, which was used to fit the experimental data (Figure 8). Error estimates for crystalline zinc phosphates: 0.1 ppm for δ_{iso}, 5 ppm for δ_{aniso}, 0.06 for η. Error estimates for as-prepared zinc-phosphate: 1.0 ppm for δ_{iso}, 10 ppm for δ_{aniso}, 0.1 for η. α-$Zn_3(PO_4)_2$,[57] β-$Zn_3(PO_4)_2$,[37] α-$Zn_2P_2O_7$, [58] and γ-$Zn_2P_2O_7$[59] were identified by XRD on samples in powder form.

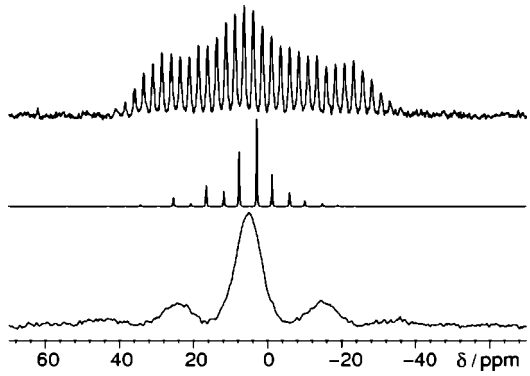

Figure 8. ^{31}P MAS NMR spectra of α-$Zn_3(PO_4)_2$ (top), β-$Zn_3(PO_4)_2$ (middle), and as-prepared zinc-phosphate nanoparticles (bottom) at a sample spinning frequency of 499, 1802, and 3980 Hz, respectively, and a magnetic field of 11.74 T.

oxygen atoms attached to a phosphorus atom.[39,40] For completeness, we have also determined the chemical shift values and T_1-relaxation time constants for crystalline α- and β-$Zn_3(PO_4)_2$, α- and γ-$Zn_2P_2O_7$ (see Table, Figure 8 and Supporting Information). Note that the quantitative ^{31}P NMR spectrum (Figure 7) contained no sharp components in the line shape, which would be expected for a small nanocrystalline core. Moreover, no appreciable change in the line shape between a cross-polarization ^{31}P{^{1}H} spectrum and a ^{31}P{^{1}H} spectrum with direct excitation was observed, which indicates that only a negligible amount of α- and β-$Zn_3(PO_4)_2$ could have been present.

^{1}H/^{31}P-DQ-2D. Double-quantum (DQ) filtered 2D correlation experiments are a powerful means to probe the homonuclear connectivity pattern in amorphous samples. For a homogeneous amorphous sample, all atoms should show connectivity, i.e., correlation peaks. This is exactly what we observed in the ^{1}H−^{1}H 2D double-quantum single-quantum correlation spectrum of as-prepared zinc-phosphate (Figure 9.) All ^{1}H resonances correlate among themselves. Interesting is also a ^{31}P−^{31}P double-quantum single-quantum correlation spectrum. A lentils-shaped 2D line shape was observed which is typical for a model with two coupling sites A, A′ being governed by the same chemical shift distribution function, which is perfectly uncorrelated: if $p_A(\delta)$ is the probability for a nucleus to have a chemical shift δ, than the intensity in a DQ filtered 2D spectrum is determined by the product of the distribution of the coupling nuclei $p(\delta_{F2},\delta_{F1}) \propto p_A(\delta_{F2})\, p_A(2\delta_{F1}-\delta_{F2})$. This description applies only when the line shape is dominated by the distribution of bond-angles and bond-distances, such that selective excitation would be able to burn a sharp hole into the line shape. This situation applies to the presented case (see the Supporting Information).

^{1}H−^{31}P 2D HETCOR. The heteronuclear connectivity pattern over less than a nanometer was accessed via a ^{31}P{^{1}H} 2D heteronuclear correlation (HETCOR) experiment based on ramped cross-polarization (Figure 10). Dipolar contacts between all ^{1}H and ^{31}P peaks are evidenced by strong correlation signals between all pairs of ^{1}H and ^{31}P peaks at a contact time of 2 ms. For shorter (0.48 ms) or longer (5 ms) contact times we did not observe a significant change of the relative peak intensities, which indicates that the individual distances between different atom pairs, hydrogen−phosphorus, are not significantly different and/or strong homonuclear spin-diffusion exists. Based on this result, qualitatively the core shell model can be rejected. Still, it would be interesting to determine an upper limit for the size of a hydrogen-free zinc phosphate core particle and give a length scale to the homogeneity of sample composition.

^{1}H−^{31}P C-REDOR. To quantitatively access heteronuclear ^{1}H−^{31}P distances it is necessary to suppress ^{1}H−^{1}H direct dipole−dipole couplings. This can be achieved with the C-REDOR[41,42] sequence, a variant of the rotational echo double resonance (REDOR) experiment.[43] Because of its small chemical shift anisotropies, ^{1}H and ^{31}P C-REDOR of amorphous zinc phosphate is ideally suited to determine such distance constraints. The initial regime ($\Delta S/S_0 < 0.2$, $\Delta S = S_0 - S$) was analyzed in a two-spin approximation that led to a dipole−dipole coupling constant ν_{dip} of −1950 Hz (Figure 11.) The intensity S_0 is the intensity measured for a spin−echo. The intensity S is the intensity of the dephased echo. The dipole−dipole coupling constant in hertz is

$$\nu_{dip} = \frac{-\mu_0}{8\pi^2}\frac{\gamma_i\gamma_j}{r^3}\hbar \qquad (1)$$

where r is the internuclear distance and γ_i/γ_j the gyromagnetic ratios of the coupling nuclei. This dipole−dipole coupling constant needs to be compared with the effective dipole−dipole coupling constant ν_{eff}, which is calculated from the sum of all squared dipole−dipole coupling constants

(41) Chan, J. C. C.; Eckert, H. *J. Chem. Phys.* **2001**, *115*, 6095.
(42) Chan, J. C. C. *Chem. Phys. Lett.* **2001**, *335*, 289.
(43) Gullion, T.; Schaefer, J. *J. Magn. Reson.* **1989**, *81*, 196.

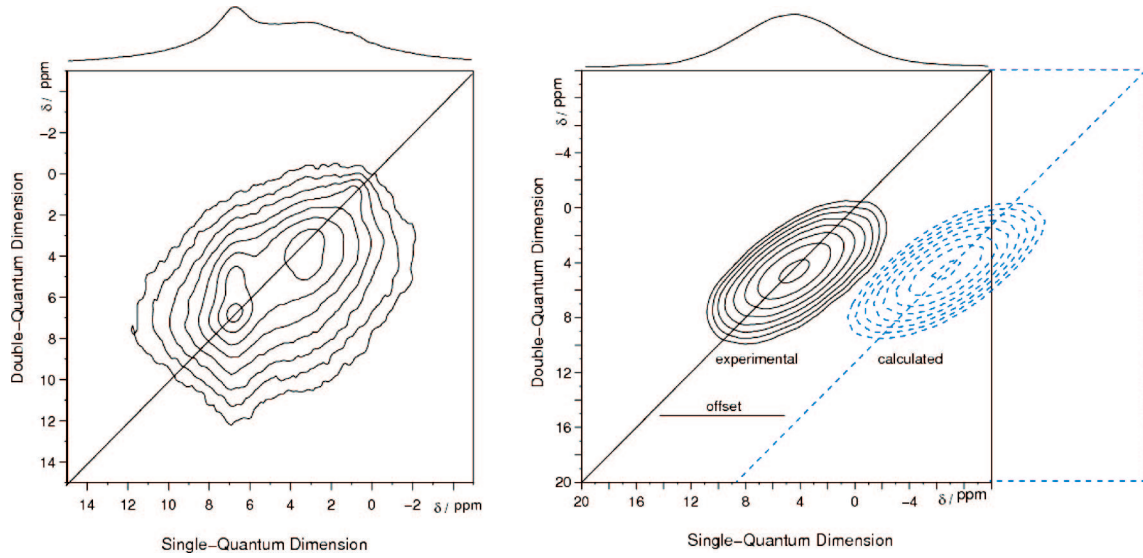

Figure 9. Homonuclear double-quantum (DQ) filtered correlation spectra: (left) ^{1}H NMR 2D DQ filtered correlation spectrum at a MAS frequency of 25 kHz using BABA and a DQ conversion time of 2 rotor periods at a magnetic field of 4.7 T, (right) ^{31}P NMR 2D DQ filtered correlation spectrum based on PostC7[56] with ^{1}H decoupling, cross-polarization, and a DQ conversion time of 2 ms at a spinning frequency 10 kHz and magnetic field of 4.7 T. The offset peak was calculated assuming an uncorrelated scenario as described in the text.

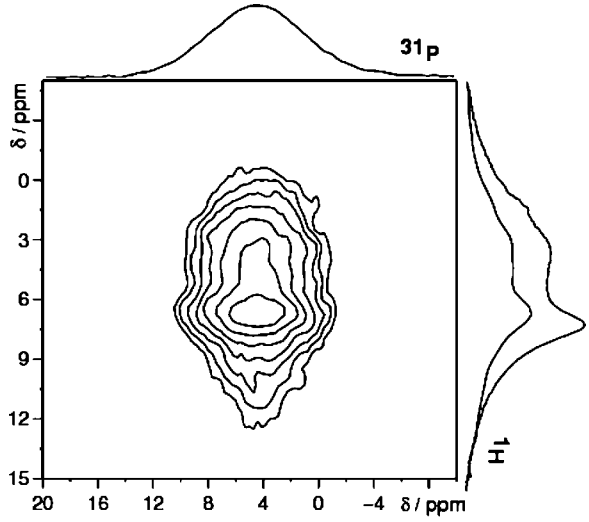

Figure 10. 2D ^{31}P{^{1}H} NMR HETCOR spectrum of as-prepared amorphous zinc phosphate based on a ramped cross-polarization experiment, acquired at a sample spinning frequency of 20 kHz at a magnetic field of 4.7 T. The projections were taken from separate 1D single-pulse excitation experiments; additionally, a sum projection of the 2D HETCOR projection is shown for the ^{1}H dimension.

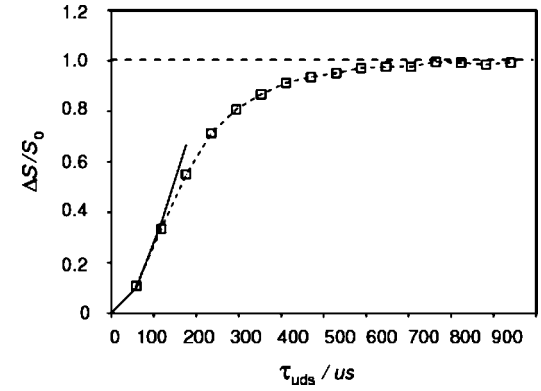

Figure 11. ^{31}P−^{1}H NMR C-REDOR curve, ^{31}P observed, squares denote experimental data points (dashed lines serve as guide to the eye); the solid line is a calculated curve for 2 spin-system with a dipole−dipole coupling constant of - 1950 Hz, at a sample spinning frequency, of 25 kHz and a magnetic field of 4.7 T.

from the observed spin ^{31}P nucleus j to all surrounding ^{1}H nuclei i. Its sign is chosen according to the sign of the individual dipole−dipole coupling constants. Apart from a constant factor, the effective dipole−dipole coupling constant behaves as a heteronuclear second moment.

$$|\nu_{\text{eff}}| = \sqrt{\sum_i \nu_{ij}^2} \qquad (2)$$

The experimental value may be compared with typical values for di-, monohydrogen phosphates or phosphate hydrates in bulk, e.g., for crystalline RbH_2PO_4,[44] ν_{eff} is −6.7 kHz; for the HPO_4 group in $Na_2HP_3O_9$,[45] ν_{eff} is −5.1 kHz; and for $Na_3P_3O_9$ $6H_2O$,[46] ν_{eff} is −4.7, −3.9, and −4.1 kHz, which can be calculated from the internuclear distances known from their crystal structures. Because of uncertainties in the proton dynamics, the magnitude of the experimental value should be considered a lower limit for the magnitude of the real value of the dipole−dipole coupling constant which could be calculated from the distances of a static model. Clearly hydrogen−phosphorus distances in a two-spin model need to be around 292 pm in order to explain the steep C-REDOR curve, while bulk values for the magnitude of the effective dipole−dipole coupling usually found for mono- or dihydrogen phosphates are too big to explain the experimental findings. Note that hydrogenated orthophosphates would also lead to diphosphates after calcination and not to the observed $Zn_3(PO_4)_2$. A quantitative evaluation of REDOR curves as a function of a nanoparticle's radius follows below.

(44) Mattauch, S.; Heger, G.; Michel, K. H. *Phys. Status Solidi A* **1990**, *122*, 117.

(45) Averbuch-Pouchot, M. T.; Guitel, J. C.; Durif, A. *Acta Crystallogr., Sect. C* **1983**, *39*, 809.

(46) Tordjman, I.; Guitel, J. C. *Acta Crystallogr., Sect. B* **1976**, *32*, 1871.

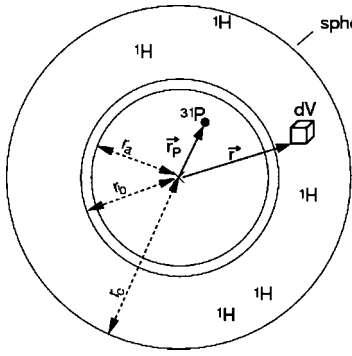

Figure 12. Cylindrical/spherical topologies for which effective dipole−dipole coupling constants have been calculated.

C-REDOR Curves For Simple Topologies. How does the experimental C-REDOR curve compare with the core−shell models discussed above? How big can the hydrogen-free core of a zinc phosphate nanoparticle be, which is covered by DEG and water?

The initial regime of a C-REDOR curve depends only on the effective dipole−dipole coupling constant if the C-REDOR curve is plotted on the universal dephasing scale τ_{uds} (see Experimental Section). For an amorphous sample, the expected C-REDOR curve may be calculated by integration of the C-REDOR curves over the probability density function of the effective dipole−dipole coupling constant $p(\nu_{eff})$.

$$\overline{\Delta S/S_0(\tau_{uds})} = \int_{-\infty}^{+\infty} p(\nu_{eff})\Delta S/S_0(\tau_{uds}, \nu_{eff})d\nu_{eff} \qquad (3)$$

Hence the task is to describe the effective dipole−dipole coupling and its probability density function. For an amorphous sample the effective dipole coupling constant is related to the summed squares of the coupling of the observed nucleus to all recoupled nuclei. The spin density of the recoupled nuclei ρ_{rec} may be used to approximate the probability to find a recoupled nucleus in a volume element. With the help of the spin density of the recoupled nuclei the effective dipole−dipole coupling may be written as

$$|\nu_{eff}(\vec{r}_P)| = \sqrt{\int \rho_{rec}\nu_{dip}^2(\vec{r} - \vec{r}_P)\mathrm{d}V} \qquad (4)$$

where $\nu_{dip}(\vec{r})$ is the dipole−dipole coupling constant to a recoupled nucleus at the position $\vec{r}$.

Thus the effective dipole−dipole coupling constant in the center of a spherical shell becomes

$$|\nu_{eff}| = K\sqrt{\frac{4\pi}{3}\rho_{rec}}\sqrt{\frac{1}{r_b^3} - \frac{1}{r_c^3}} \qquad (5)$$

in the center of a cylindrical shell

$$|\nu_{eff}| = K\sqrt{\frac{\pi}{4}\rho_{rec}}\sqrt{\frac{1}{r_b^3} - \frac{1}{r_c^3}} \qquad (6)$$

and close to a planar topology of recoupled nuclei as indicated in Figure 12

$$|\nu_{eff}| = K\sqrt{\frac{\pi}{6}\rho_{rec}}\sqrt{\frac{1}{r_b^3} - \frac{1}{r_c^3}} \qquad (7)$$

The latter two formulas might become interesting for C-REDOR curves of nanosized fibers or plates. In the above eqs 5, 6, and 7, the constant K equals $\mu_0(8\pi^2)\gamma_i\gamma_j\hbar$.

To calculate the C-REDOR curve for the core shell model, the following integral equation for a spherical model needs to be evaluated. The distance is $r_b - r_a$, the minimum distance between a hydrogen nucleus and a phosphorus nucleus (Figure 12). For phosphate hydrates, this is approximately 292 pm.

$$\overline{\Delta S/S_0(\tau_{uds})} = \int_0^{r_a} dr_P p(r_P)\Delta S/S_0(\tau_{uds}, \nu_{eff}) \qquad (8)$$

The probability density function is

$$p(r_P) = \frac{3r_P^2}{r_a^3} \qquad (9)$$

A similar treatment has recently been published by Schmidt-Rohr and co-workers.[14] Their formulas also show the inverse cube of distance dependency for the second moment alias effective dipole−dipole coupling. We have determined the C-REDOR curves for nanoparticles with various diameters (Figure 13) by evaluating eqs 4, 8, and 9 numerically, because we did not find a closed analytical expression. The hydrogen spin density was approximated from ice-II,[47] which is close to that of DEG. The core shell model with a radius of 10 nm would not explain the experimental curve. Within this model the smallest nanoparticle still in agreement with the experimental data and with complete coverage by DEG/H_2O would have a radius of 1.6 nm. Clearly, the homogeneous core-free model offers a better explanation and a description consistent with all experimental data.

Conclusions

The polyol-mediated synthesis again turned out to be well-suited for the realization of almost monodispersed and nonagglomerated nanoparticles. The mean diameter of as-prepared zinc phosphate was measured to 20 nm applying independent and state-of-the-art methods of characterization, namely SEM, TEM, XRD, DLS, and BET. In contrast to several recently published nanomaterials[26−29] prepared with the same concept of synthesis, here, XRD, HRTEM, and SAED show as-prepared nanoparticles to be non-crystalline. According to averaging analytical tools—XRD, SAED, FT-IR, EXD, DTA-TG—the chemical composition of noncrystalline zinc phosphate results approximately to $Zn_3(PO_4)_2 \cdot 0.3$

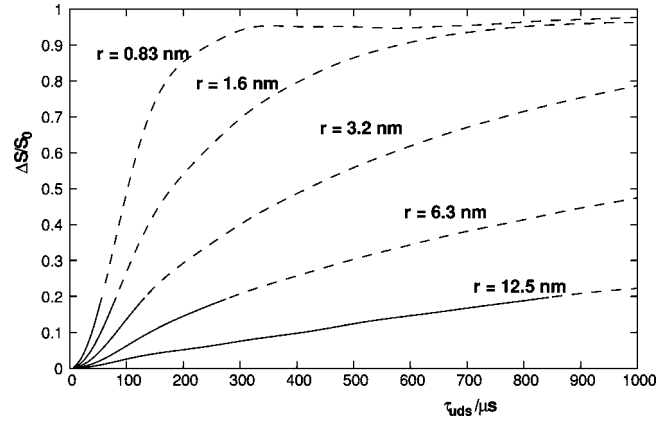

Figure 13. Calculated $^{31}P-^{1}H$ NMR C-REDOR curves for hydrogen-free nanospheres with different radii covered by water; solid lines indicate that $\Delta S/S_0$ is below the limit of the initial regime.

DEG·0.7 H_2O. The aspired composition $Zn_3(PO_4)_2$ was indeed confirmed subsequent to annealing of as-prepared samples. On a local scale, solid-state NMR clearly showed that as-prepared zinc phosphate is a homogeneous precipitate consisting of water, DEG, zinc ions and orthophosphate groups. A model based on a $Zn_3(PO_4)_2$ core covered by DEG and/or water does not agree with the experimental findings. Quantitative constraints imposed by $^{31}P\{^1H\}$ C-REDOR experiments give an upper limit for a hydrogen-free particle core of 1.6 nm, the length-scale of homogeneity, and allow us to differentiate between phosphate hydrates and mono- and dihydrogenphosphates.

Our results indicate that the polyol-mediated synthesis of nanomaterials may strongly be influenced by the chelating effect of the chosen polyol. In the special case presented here, Zn^{2+}−DEG complexes embedded in PO_4^{3-} seem to be more stable than a phase-separated DEG/H_2O/$Zn_3(PO_4)_2$. Future work will show how the delicate equilibrium between the chelated cation and a polyol-free nanoparticle may be controlled by chemical means. The application of independent analytical tools altogether turned out to be very versatile in order to verify composition and structure even of noncrystalline nanomaterials.

Experimental Section

Synthesis. In a typical recipe for the polyol-mediated synthesis of nanoscale zinc phosphate, DEG (50 mL, 99%, Acros) was placed in a three-neck flask (volume 100 mL) with a Claisen stillhead. The synthesis was performed with a continuous nitrogen flow and vigorous stirring. Zinc acetate dihydrate (111 mg/0.51 mmol, 99.999%, Sigma−Aldrich) was added and dissolved at 110 °C (solution 1). In addition, $NH_4H_2PO_4$ (39 mg/0.34 mmol, 99.5% Fluka) was dissolved in deionized water (0.5 mL) at room temperature (solution 2). Solution 1 was cooled to 50 °C and solution 2 was rapidly added. After 15 min of stirring, the suspension was rapidly heated (within 5 min) to 150 °C for 10 min in order to distill off water. Then a reflux condenser was mounted and the suspension was heated at 230 °C under N_2 flow for additional 45 min. To separate the solid material, we added ethanol (50 mL) and centrifuged the suspension (20 min, 26000 rpm). Thereafter, the solid was resuspended in and centrifuged from ethanol three times, in order to remove all DEG and remaining salts. Finally, the product was dried in a drying oven (15 min, 75 °C). The nanoscaled solid can be easily redispersed in DEG by sonification.

Fundamental Characterization. Dynamic light scattering (DLS) was conducted with polystyrene cuvettes applying a Nanosizer ZS (Malvern Instruments). Samples were measured after resuspension in DEG. Scanning electron microscopy (SEM) was carried out on a Zeiss Supra 40 VP equipped with a field-emission gun (samples were sputtered with Pt, acceleration voltage 10 kV, working distance 3 mm). Transmission Electron Microscopy (TEM) was performed with a Philips CM 200 FEG/ST device (samples on a carbon-coated copper grid, preparation via vacuum evaporation of particle dispersions in DEG at 120 °C, acceleration voltage 200 kV). Brunauer−Emett−Teller (BET) analysis was performed via N_2 adsorption with a Belsorp-mini apparatus. The sample was vaccuum-dried for 3 h at room temperature. Energy-dispersive X-ray analysis (EDX) was carried out on an AMETEC EDAX mounted at the Zeiss SEM. Powder samples were pressed to pellets, which were then fixed with conductive carbon pads on aluminum sample holders. Fourier-transform infrared (FT-IR) spectra were recorded with a Bruker Vertex 70 FT-IR spectrometer; the samples were measured in KBr with a resolution of 4 cm^{-1}. Differential thermal analysis (DTA) and thermogravimetry (TG) were performed on a Netzsch STA 409 C. The samples were deposited in alumina crucibles and heated in air from 20 to 700 °C at a heating rate of 10 K min^{-1} and a flow rate of 2 mL min^{-1}. X-Ray powder diffraction (XRD) measurements were conducted with a Stoe Stadi P system using monochromated Cu Kα radiation.

Solid-State NMR. Experiments were performed at 4.7 T on Bruker Avance II-200 spectrometer equipped with a commercial 2.5 mm double resonance MAS probe at a ^{31}P and ^1H frequency of 81.032 and 200.175 MHz, respectively. However, ^{31}P slow MAS NMR experiments were performed on a Bruker DSX 500 spectrometer at a ^{31}P Larmor frequency of 202.5 MHz with a commercial 4 mm triple-resonance MAS. The chemical shifts of ^1H, ^{13}C and ^{31}P were reported using the δ scale, relatively to 1% tetramethylsilane (TMS) in $CDCl_3$ and 85% H_3PO_4.[48] Typically, a contact time τ_{CP} of 2−5 ms for cross polarization experiments was used for all experiments. The nutation frequencies of the decoupling rf field applied to ^1H ranged from 97 to 122 kHz. Saturation combs were applied prior to relaxation delays in all experiments. The one-dimensional (1D) ^1H NMR spectrum was acquired with a 90° pulse length of 2.5 μs, recycle delay (τ_{RD}) of 10 s and at sample spinning frequency of 25 kHz. Similarly, ^{31}P magic-angle spinning NMR spectra were obtained with direct excitation (MAS) at a spinning speed 10 kHz with a pulse length of 2.5 μs and a recycle delay of 8.0 s as well as ramped cross polarization with MAS.[49] The 2D $^1H-^1H$ double-quantum (DQ) filtered correlation spectrum was acquired at a sample spinning frequency of 25 kHz. The DQ MAS experiments were performed with a 12 step cogwheel phase cycle[50] Cog12(2,5,6;0) of the back-to-back (BABA) recoupling sequence.[51−53] During all 2D correlation experiments we used rotor synchronized t_1 increments and 2D data acquisition according to the States method.[54] The 2D heteronuclear correlation spectrum was performed using a $^{31}P\{^1H\}$ ramped cross polarization at a spinning frequency 20 kHz.[38] For the ^1H spin lock a nutation frequency of 88.48 kHz and a 10% ramp were applied. C-REDOR experiments were based on $CX^1{}_X$ ($X \in N$, $X > 1$) symmetry and POST C elements ($C = \{90_0, 360_{180}, 270_0\}$, pulse notation flip-angle$_{phase}$ both in degrees) at a spinning frequency of 25 kHz. The rf field strength employed during $CX^1{}_X$ on the ^1H channel was set to 50 kHz. 128 transients were accumulated for each measurement.[41,42] The C-REDOR data were plotted following standard REDOR notation as $\Delta S/S_0$ against dephasing time τ. To get a pulse sequence independent time-scale, we introduce the universal dephasing scale τ_{uds}, which is defined as the product of the magnitude of the scaling factor κ times the dephasing time τ; here, κ equals 0.24503 for $CX^1{}_X$ with a POST C element.

$$\tau_{uds} = |\kappa|\tau \tag{10}$$

The universal dephasing scale has the advantage that different REDOR experiments, for example the simple REDOR and the C-REDOR experiment, yield the same curve for the same

(47) Kamb, B. *Acta Crystallogr.* **1964**, *17*, 1437.
(48) Harris, R. K.; Becker, E. D. *J. Magn. Reson.* **2002**, *156*, 323.
(49) Metz, G.; Wu, X.; Smith, S. O. *J. Magn. Reson.* **1994**, *A110*, 219.
(50) Levitt, M. H.; Madhu, P. K.; Hughes, C. E. *J. Magn. Reson.* **2002**, *155*, 300.
(51) Feike, M.; Demco, D. E.; Graf, R.; Gottwald, J.; Hafner, S.; Spiess, H. W. *J. Magn. Reson.* **1996**, *A122*, 214.
(52) Feike, M.; Graf, R.; Schnell, I.; Spiess, H. W. *J. Am. Chem. Soc.* **1996**, *118*, 9631.
(53) Graf, R.; Demco, D. E.; Gottwald, J.; Hafner, S.; Spiess, H. W. *J. Chem. Phys.* **1997**, *106*, 885.
(54) States, D. J.; Haberkorn, R. A.; Ruben, D. J. *J. Magn. Reson.* **1982**, *48*, 286.

dipole−dipole coupling constant. Fitting of the initial part of the C-REDOR curve and numerical simulations of MAS NMR-spectra were carried out using the SIMPSON package.[55] Other essential experimental parameters are listed in the figure captions.

Acknowledgment. M.R. and C.F. are grateful to the Center for Functional Nanostructures (CFN) of the Deutsche Forschungsgemeinschaft (DFG) at the University of Karlsruhe (TH) for financial support and to Prof. Dr. D. Gerthsen and Dipl.-Phys. W. Send, Laboratorium für Elektronenmikroskopie der Universität Karlsruhe (TH), for TEM analysis. J.S.a.d.G. and Y.S.A. gratefully acknowledge financial support through the Emmy-Noether program of the DFG (SCHM1570-2/1), Munich University (LMU) and by the "Fonds der deutschen chemischen Industrie". The authors thank Prof. Dr. R. Glaum and Dr. F. Reinauer for providing the crystalline zinc diphosphates.

Supporting Information Available: $^{13}C\{^1H\}$ cross-polarization MAS NMR spectrum, $^{13}C\{^1H\}$ HETCOR spectrum, ^{31}P 2D exchange spectrum with zero mixing time of zinc phosphate nanoparticles, and ^{31}P MAS NMR spectra of crystalline α-$Zn_2P_2O_7$ and γ-$Zn_2P_2O_7$ (PDF). This material is available free of charge via the Internet at http://pubs.acs.org.

CM800805F

(55) Bak, M.; Rasmussen, J. T.; Nielsen, N. C. *J. Magn. Reson.* **2000**, *147*, 296.
(56) Hohwy, M.; Jakobsen, H. J.; Edén, M.; Levitt, M. H.; Nielsen, N. C. *J. Chem. Phys.* **1998**, *108*, 2686.
(57) Calvo, C. *Can. J. Chem.* **1965**, *43*, 436.
(58) Karimova, O. V.; Yakubovich, O. V.; Urusov, V. S. *Vestn. Mosk. Univ., Ser. 4: Geol.* **1997**, *52*, 35.
(59) Bataille, T.; Bernad-Roucherulle, P.; Louer, D. *J. Solid State Chem.* **1998**, *140*, 62.